



Contents lists available at ScienceDirect

Particuology

journal homepage: www.elsevier.com/locate/partic

Particle size and shape analyses for powder bed additive manufacturing

Langdon Feltner, Ethan Korte, David F. Bahr, Paul Mort*

School of Materials Engineering, Purdue University, West Lafayette, IN, USA

ARTICLE INFO

Article history:

Received 17 July 2023

Received in revised form

23 August 2023

Accepted 4 September 2023

Available online xxx

Keywords:

Dynamic image analysis

Powder bed additive manufacturing

Clustering of particle shape descriptors

Pixilation

Machine learning

ABSTRACT

Technical advances in dynamic imaging have enabled routine sampling and analysis of particle shape and shape distributions. Size and shape distributions are relevant to many particulate processes involving flow, spreading, packing and densification. Powder bed additive manufacturing is a prime example requiring uniform spreading, packing and sintering of fine metal powders. This study focuses on quantitative representations of shape described in the International Standards Organization specifications and considers three aspects for improvement thereof: (1) reduced-order mapping of shape distributions using principal component analysis of shape descriptors; (2) uncertainty of shape distribution statistics based on pixel resolution; and (3) opportunities for analysis using machine learning for enhanced image resolution.

© 2023 Chinese Society of Particuology and Institute of Process Engineering, Chinese Academy of Sciences. Published by Elsevier B.V. All rights reserved.

1. Introduction

This is a case study of particle size and shape analysis using dynamic imaging of two powdered metal samples intended for use in powder bed fusion (PBF), a method of additive manufacturing (AM). One sample was produced by melt atomization and the other by cold mechanical processing, a precise size-reduction process. The methods of production affect the size and shape distributions. Classification of particles improves the reproducibility of PBF processes, as particle size and shape impact steps from powder flow to bed packing to optical interactions with lasers used to locally melt the material. Particle image data were collected using a commercial Dynamic Imaging Analysis system described in Section 2. The raw data, in the form of 8-bit grayscale digital images, were analyzed in more detail to determine the effects of pixel-scale resolution (i.e., the number of pixels per particle) on shape descriptors. We compare and contrast the data for each sample and consider the effect of pixel-scale resolution on the comparison.

A principal component analysis (PCA) of shape descriptors showed that over 90% of differences within the samples used in this study were explained using two components: one indicating elongated shape (i.e., aspect ratio) and another indicating features associated with perimeter length in excess of a smooth ellipse. Subjectively, excess perimeter length can manifest as bumpiness or

angularity. The International Standards Organization (ISO)-standard form factor (ISO, 2008) captures a combination of the two effects and can be used to indicate about 60% of the differences using a single shape factor. This study includes a detailed analysis of pixel-scale resolution on principal shape descriptors.

Characterization of porosity is important in many applications. Porosity can be associated with individual particles (intra-particle, ϵ_{tra}) as well as interstitial voids in an ensemble packing (inter-particle voids, ϵ_{ter}). Metal powder AM can meet a range of structural objectives requiring control and manipulation of porosity (Slotwinski, Garboczi, & Hebenstreit, 2014). Often the objective is to make fully dense structures, i.e., the total elimination of porosity. In other cases, for example, bio-medical implants, some residual porosity may be desired. While the effects of closed intra-particle porosity, $\epsilon_{tra,closed}$, for example, as a consequence of trapped gas in an atomization process, have been traced to defects in AM parts (Anderson, White, & Dehoff, 2018), there is comparatively little work on the effects of particle shape on spreading and packing in powder-bed processes (Shaheen, Thornton, Luding, & Weinhart, 2021). Intra-particle porosity that is related to concavity, $\epsilon_{tra,open}$, may be useful in correlating shape with spreading and packing. This study explores the relationship between intra-particle porosity and perimeter concavity that is detectable with 2D image analysis. Machine learning (ML) for fine-grain image reconstruction is discussed in this context.

The results and discussion of principal component analysis and mapping of orthogonal shape descriptors are covered in sections

* Corresponding author.

E-mail address: pmort@purdue.edu (P. Mort).

4.1 through 4.3. Section 4.4 covers the effect of pixel resolution on shape analysis, first on the basis of individual particles (section 4.4.1) and then on a distributed ensemble basis (section 4.4.2). Enhancement of shape resolution using ML is introduced in section 4.4.1 and discussed further in Appendix B.

2. Background – image analysis

Many studies on particle image analysis are available in the literature. With advances in digital-imaging and data-processing technologies, size and shape analyses are becoming more routine for many applications (Pons & Dodds, 2015). However, given the long history of particle image analysis and its diverse applications, there remain some contradictions on terminology and analysis. For example, shape mapping is well practiced in geo-mechanics, using Krumbein–Schloss charts (Krumbein & Sloss, 1951) and variations thereof (Kim, Suh, & Yun, 2019; Zheng & Hryciw, 2015) to correlate shape distributions with stability, packing, and flow of sands and sediments. In relation to the current work, geo-technical “sphericity” is analogous to the bounding-box aspect ratio, AR_{box} ; and geo-technical “roundness” is indirectly related to an extended perimeter measure described herein as the elliptical form factor (EFF) (see details in Section 3 and Appendix A). As a starting point, this study references the guidance and terminology of the ISO (ISO, 2008).

Particle size distributions have been shown to have a significant effect on the mechanical properties and surface finish of additively manufactured parts (Spierings, Herres, & Levy, 2011; Weaver et al., 2021). There is also precedence that the morphology of the powder influences the outcome of the process (Muñiz-Lerma, Nommeots-Nomm, & Brochu, 2018; Martin et al., 2023). This has been attributed to size and shape distributions affecting the powder-spreading performance, leading to non-uniform layer thicknesses in severe cases. It is therefore critical to be able to accurately and repeatably characterize the particle size and shape distribution of additive powders consistently across the size distribution in order to predict and control an AM process.

The effect of digital image resolution and pixilation on shape results and the uncertainty thereof has been studied (Đuriš, Arsenijević, Jaćimovski, & KaluderovićRadoičić, 2016; Kröner & Doménech Carbó, 2013). These articles point out that the computation of particle perimeter, and shape factors that utilize perimeter, are especially affected by relatively coarse pixel scales. Most commonly used commercial and open-source vision packages calculate a smoothed perimeter measurement, rather than summing the total length of pixel edges (MATLAB, 2023; MorphoLibJ, 2023; NI-Vision, 2023). If not explicitly defined as such, this technique is analogous to Cauchy–Crofton smoothing (Pirard, 2004; ISO, 2008), relying on numerical integration to calculate an approximate curve length. The effect of bounding surface construction on the precision of the Cauchy–Crofton computation has also been explored, with the conclusion that irregular surfaces require a higher degree of detail to accurately compute the length or area (Daugmaudis, Laurynėnas, & Ivanauskas, 2010). The particle’s area is computed as the sum of pixels below a threshold grayscale value. When this area is compared to a smoothed perimeter, inconsistencies can arise, especially at low pixel counts, leading to a smoothed perimeter that is illogical for a measured area, i.e., having an area-to-perimeter ratio higher than that of an ideal circle. This phenomenon is an artifact of inaccurate perimeter smoothing, i.e., smoothing over an insufficient number of pixels. Overall, high resolution is desired for robust imaging and analysis; this is an inherent challenge for particle distributions having significant dispersity in size and shape features. This paper seeks to illustrate and understand the effects of image analysis uncertainty across a distributed set of size and shape characteristics.

3. Experimental methodology

Fine metal powders comprising 7075 aluminum alloy obtained from two commercial vendors were used in this study. The gas atomized (GA) sample was made by melting-gas atomization; the other sample was made via a proprietary (Barnes & Aldridge, 2019) size-reduction process (cold mechanical processing, CMP). Both were measured in a liquid-dispersion flow-through imaging system (InFlow™, JM Canty, Lockport, NY, USA) having a back-lit strobe (exposure time of 20 μ s) and an image resolution of 0.34 μ m/pixel. The back-lit imaging captures 2D projections of particles that are randomly oriented in a suspension flow, i.e., dynamic image analysis (Fig. 1). The InFlow system uses NI Vision (National Instruments, Austin, TX, USA) as a foundational platform for data acquisition and analysis of size and shape features. The InFlow software has an option to save 8-bit grayscale digital bitmaps of all particles; this was used for detailed analysis of the effects of pixilation on the shape, conducted in this study.

Samples of AM metal powders were prepared by placing ~0.5 g of metal powder in a glass vial and then adding several drops of isopropyl alcohol (IPA) as a surface-wetting agent. The IPA has a secondary function of being an anti-foam agent. About 10 mL of an aqueous diluent is added to make a suspension of the metal powder. The diluent comprised 4% hydroxypropyl cellulose (HPC Klucel, obtained from Ashland Chemical, Wilmington, DE, USA) as a thickening agent. Increasing the viscosity (~0.3 Pa s) was effective in reducing the settling speed of the particles and stabilizing the dilution control loop. The suspension was mixed by repeated syringe drawing and extraction, taking care to avoid generation of air bubbles.

At the start of the measurement, the InFlow provides a reservoir in a sample reservoir, to which the prepared suspension was added, again using the syringe to avoid generation of air bubbles. Dual peristaltic pumps are used to draw the sample suspension through the imaging cell according to a control loop objective of 0.2% screen area below the particle detection threshold. The threshold setting was 170 out of a grayscale of 0–255, i.e., pixels ≤ 170 were considered to be within a particle, pixels > 170 were considered background. Note that metals are optically opaque materials, providing good edge contrast. The inset in Fig. 2(a) shows edge discrimination at the 170 threshold; orange pixels have at least one edge, and blue pixels have at least one corner crossing the threshold.

Size and shape analyses conducted in this study are based on the following image features, illustrated in Fig. 2. Additionally, an

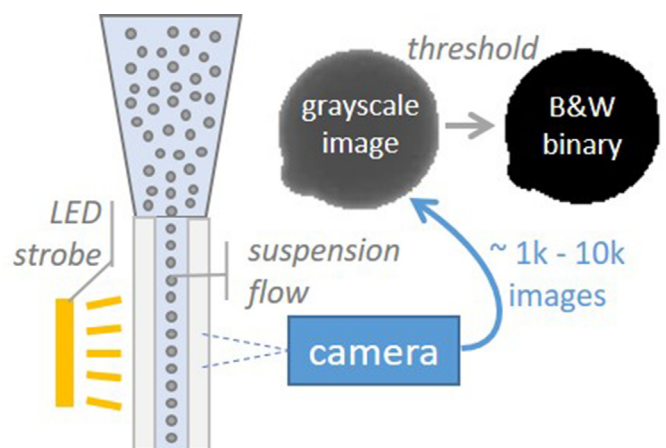


Fig. 1. Dynamic image analysis (InFlow™, JM Canty) with lab dilution controls (not shown).

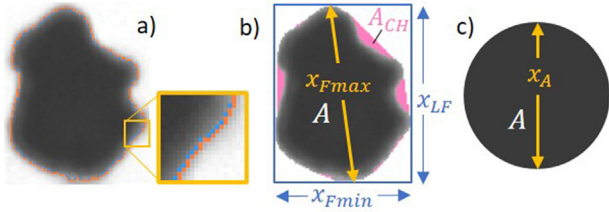


Fig. 2. Image analysis descriptors: (a) grayscale particle image with perimeter thresholding, orange = edge pixels, blue = interior edge corners; (b) thresholded image with the minimum Feret bounding box in blue, additional convex hull area in pink; (c) area-equivalent diameter. Illustrated particle data: $x_{Fmin} = 25.4 \mu\text{m}$, $x_{LF} = 33.1 \mu\text{m}$, $x_{Fmax} = 33.4 \mu\text{m}$, $x_A = 27.7 \mu\text{m}$, $A = 602 \mu\text{m}^2$, $A_{CH} = 633 \mu\text{m}^2$, $P = 95.1 \mu\text{m}$. (For interpretation of the references to color in this figure legend, the reader is referred to the web version of this article.)

estimate of intra-particle porosity, ε_{tra} , was derived using a 2D to 3D transformation of solidity. It is an estimate of concave porosity that is visually open in a 2D projection of a 3D particle, i.e., $\varepsilon_{tra,open}$, and may affect ensemble packing. It does not account for porosity that is not visible, e.g., internal pores that are effectively closed, $\varepsilon_{tra,closed}$. Going forward in this paper, all references to ε_{tra} imply $\varepsilon_{tra,open}$. Note that from a distribution analysis perspective, ε_{tra} provides a more sensitive metric than solidity.

- Area and convex-hull area: A and A_{CH} , respectively;
- Perimeter, P , based on smoothing of the pixelated edge, shown by the orange pixels in Fig. 2(a);
- Feret lengths: minimum, orthogonal to the minimum, and maximum, x_{Fmin} , x_{LF} , and x_{Fmax} respectively;
- Area-equivalent size, $x_A = \sqrt{4A/\pi}$, derived from the area A ;
- Particle volume is based on area, $V = 4A^{1.5}/(3\sqrt{\pi})$.
- Aspect ratios:
 - $AR_{box} = x_{Fmin}/x_{LF}$
 - $AR_{ISO} = x_{Fmin}/x_{Fmax}$
- Form factors: standard (ISO) and elliptical (see Appendix A for derivation):
 - $FF = 4\pi A/P^2$
 - $EFF = \beta\pi A/P^2$, $\beta = \left(\frac{1.5(1+AR_{box})}{\sqrt{AR_{box}}} - 1\right)^2$
- Area ratios per ISO guidance: Box area, Extent, and Solidity:
 - $BAR = A/(x_{Fmin} \cdot x_{LF})$
 - $Ext = A/(x_{Fmin} \cdot x_{Fmax})$
 - $S = A/A_{CH}$
- Open intra-particle porosity, $\varepsilon_{tra} = 1 - S^{1.5}$.

4. Results and discussion

4.1. Principal component analysis of particle shape

PCA of shape descriptors was used to identify clusters and rank individual shape descriptors in terms of their effectiveness in shape differentiation (JMP, SAS Institute, Cary, NC, USA). The volume-weighted PCA included the combined data of GA ($N = 5629$) and CMP ($N = 1086$) particle samples, each having equivalent total particle volumes of $7.81\text{E-}2 \text{ mm}^3$. The results showed that over 90% of shape effects can be described with two principal components (Fig. 3). Clustering of shape descriptors by principal component (Table 1) indicates characteristic features for orthogonal components, EFF and AR_{box} , respectively. Characteristic features are defined as having the highest correlation (R^2) within a given cluster and the lowest correlation with other clusters. The

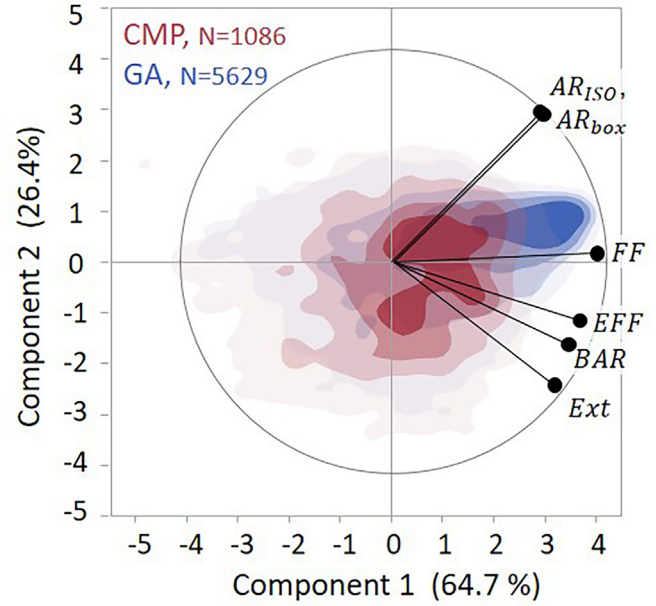


Fig. 3. Principal component analysis of shape descriptors for combined samples: gas-atomized (GA), cold mechanical processed (CMP). Color hue contours represent the data density of each sample; number of data points in legend. (For interpretation of the references to color in this figure legend, the reader is referred to the web version of this article.)

Table 1

Principal component analysis cluster summary.

Cluster	Members	R^2 within cluster	R^2 with other cluster
1	EFF	0.864	0.141
	Ext	0.810	0.018
	BAR	0.807	0.100
	FF	0.799	0.438
	AR_{box}	0.991	0.164
2	AR_{ISO}	0.991	0.169

BAR = box area; FF = form factor; EFF = elliptical form factor; Ext = extent; AR = aspect ratio.

characteristic features, EFF and AR_{box} , are used as orthogonal factors in shape mapping, section 4.3.

When shape descriptors are constrained to a single cluster, FF becomes the most representative feature; essentially, FF is a combination of EFF and AR_{box} . However, clustering all effects within a single component describes only about 65% of the shape variance. Hence, the deconstruction of the form factor into elongation and perimeter effects provides a substantial improvement in the statistical description of particle shape.

4.2. Size and shape distributions

Size distribution analysis was done using the weighted regression method (Mort, 2022). The log-normal fits reveal significant differences in size distributions of the two samples (Fig. 4), where the fit parameters relate to cumulative distribution functions (cdf_{LN}) per Eq. (1). Compared to the GA sample, CMP is larger in size and is narrower in distribution when viewed as a volume-basis distribution (Fig. 4(a)). The number-basis distribution has a bimodal fines tail in the CMP sample but not in GA. While the CMP processing and any subsequent classification step is apparently highly efficient on a volume basis, the number distribution reveals a trace residue of fines; this is typical of a milling-classification process.

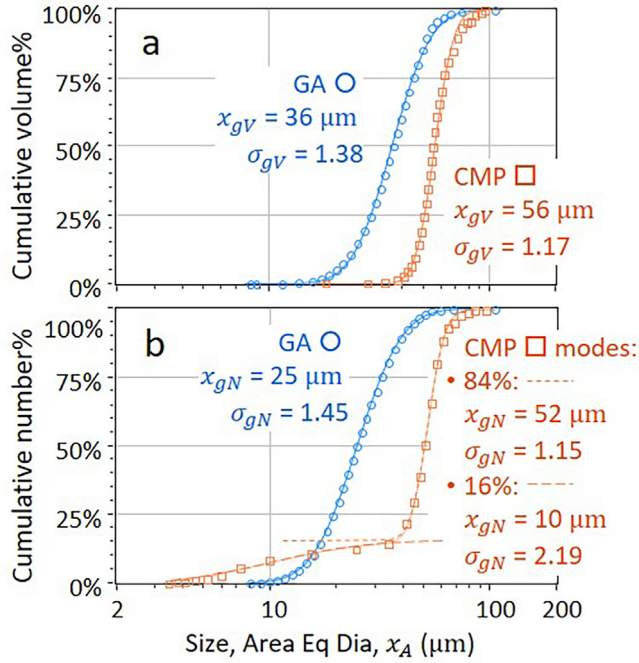


Fig. 4. Size distributions with log-normal fitting parameters for gas-atomized (GA) and cold mechanical processed (CMP) samples: (a) volume; (b) number basis.

Table 2

Fit parameters for bimodal stretched-exponential shape distributions shown in Fig. 5; gas-atomized or cold mechanical processed samples.

Sample	Mode	AR_{box}			EFF			FF		
		vol%	x^*	n	vol%	x^*	n	vol%	x^*	n
GA	1	63%	0.87	9.7	47%	0.93	18.6	33%	0.93	18.2
	2	37%	0.64	7.3	53%	0.82	7.9	67%	0.80	6.8
CMP	1	86%	0.78	6.4	60%	0.9	26.3	77%	0.86	17.3
	2	14%	0.62	10.7	40%	0.81	10.2	23%	0.67	10.2

CMP = cold mechanical processed; GA = gas atomized; AR = aspect ratio; EFF = elliptical form factor; FF = form factor.

$$cdf_{LN} = \frac{1}{2} \cdot \left(1 + \operatorname{erf} \left(\frac{\ln(x/x_g)}{\sqrt{2} \cdot \ln(\sigma_g)} \right) \right) \quad (1)$$

The weighted regression method was also used to analyze shape distributions. Shape factors are dimensionless and are bounded between 0 and 1 (0, 1]. Bimodal stretched-exponential distribution (i.e., Weibull) functions were used to model the shape data. Fit parameters in Table 2 describe the shape distributions according to Eq. (2), where the modes are summed to describe stretched-exponential cumulative distribution functions (cdf_{SE}) on a volume basis. The density plots (Fig. 5) are the derivatives of the cumulative data with respect to $\ln(x)$.

$$cdf_{SE} = 1 - \exp \left(- \left(x/x^* \right)^n \right) \quad (2)$$

Comparing the two samples, the GA sample has marginally higher mode values (x^*) for all three features indicating a more rounded morphology; however, there is broad overlap over the full distributions. The CMP sample has discernably sharper peaks (higher weighted n) within the density distributions, suggesting the process creates a tight distribution.

4.3. Shape mapping

The orthogonal relationship between aspect ratio and the elliptical form factor enables graphical mapping of shape factors using contours (Fig. 6). A value of (1, 1) is a circle, i.e., a 2D projection of a spherical particle. Decreasing values along the ordinate correspond to shape elongation, i.e., a reduced aspect ratio. Decreasing abscissa values indicate perimeter length in excess of a smooth ellipse; reduction in EFF can manifest as subjective features such as bumpiness or angularity. Grayscale contours (z-axis) indicate sample density (darker is higher density), weighted according to a distribution basis or moment, e.g., the volume bases shown in Fig. 6 were calculated from the accumulated volume of particles in each sample's (x , y) domain.

Colored contour lines show selected form factor quantiles for each sample. Recall, the form factor shows the effect of having a perimeter length in excess of a circle of the same area. It combines both perimeter irregularity and elongation into a single shape descriptor but does not distinguish between each effect. For example, in Fig. 6(b), particles labeled B and D are both close to the median form factor, FF_{50} , yet B is elongated and relatively smooth, and D is equiaxed and comparatively bumpy.

Each map is illustrated by thresholded grayscale images showing differences and trends for each sample. Objectively, shape

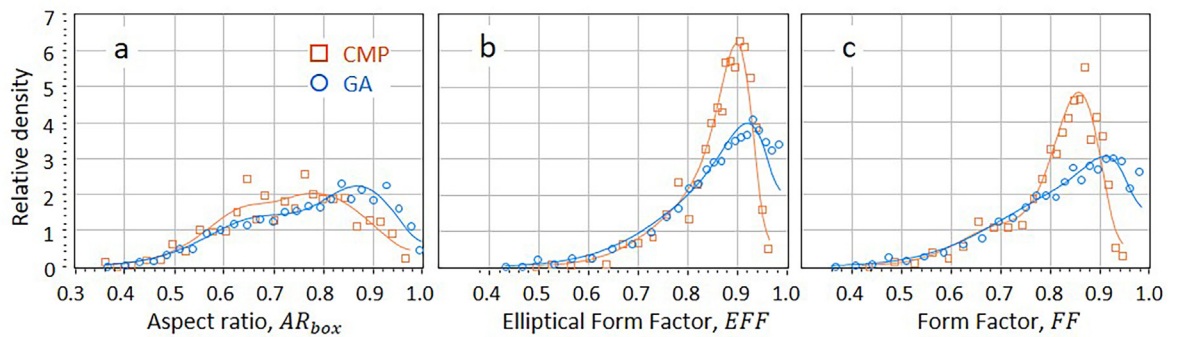


Fig. 5. Volume-basis shape distributions: (a) aspect ratio, (b) elliptical form factor, (c) form factor.

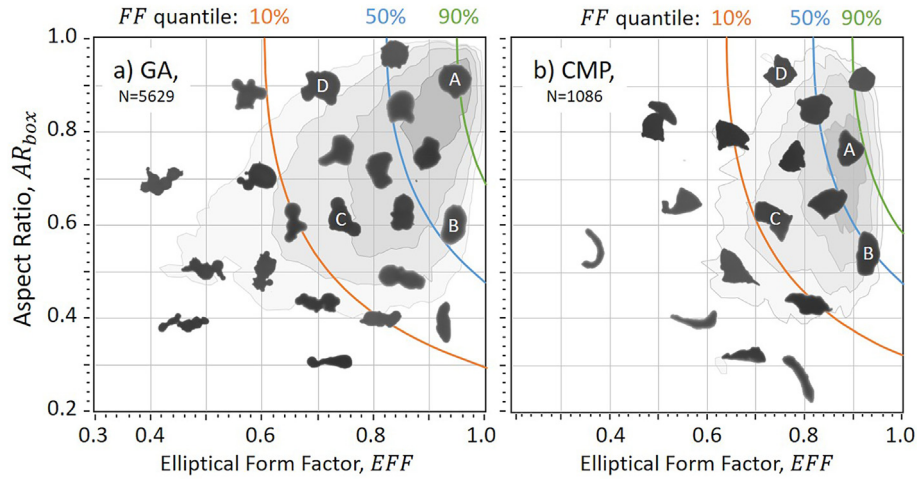


Fig. 6. Shape feature mapping: (a) gas-atomized (GA), (b) cold mechanical processed (CMP) particles. Volume-basis density indicated by grayscale contours. Tagged particles (A, B, C, D) are used for detailed analysis of pixel resolution shown in Fig. 8.

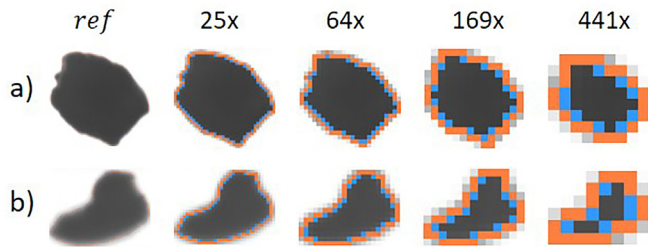


Fig. 7. Coarse graining by area of gray-scale images with perimeter threshold pixels in color (orange edges, blue interior corners), representing cold mechanical processed (CMP) shape distribution modes: (a) $AR_{box} = 0.78$, $EFF = 0.90$; (b) $AR_{box} = 0.62$, $EFF = 0.81$. (For interpretation of the references to color in this figure legend, the reader is referred to the web version of this article.)

factors in and of themselves do not necessary differentiate between samples, i.e., GA versus CMP. Visual imaging adds value to the analysis, in this case, offering visual evidence of the effects of different manufacturing processes.

4.4. Pixel-scale resolution

In the earlier analysis, particles have relatively high pixel resolution, i.e., per ISO guidance (ISO, 2008) of at least 5000 pixels/particle for robust shape analysis with factors requiring perimeter measurement. In the GA sample, the number and volume-weighted geometric averages were 4300 and 8800 pixels/particle, respectively. In the CMP sample, it was 11,800 and 22,400, respectively. High-resolution imaging provides confidence in shape analysis. In this part of the study, we investigate the effect of pixel resolution on shape analysis. Taking the high-resolution data as a reference, systematic coarse-graining was done to reduce linear pixel-scale resolution, following a Fibonacci sequence: 2, 3, 5, 8, 13, 21 ..., resulting in areal reduction of pixel resolution by factors of 4, 9, 25, 64, 169, and 441+, to a limit of about 10 pixels/particle. Coarse graining is illustrated in Fig. 7 using two example particles from the

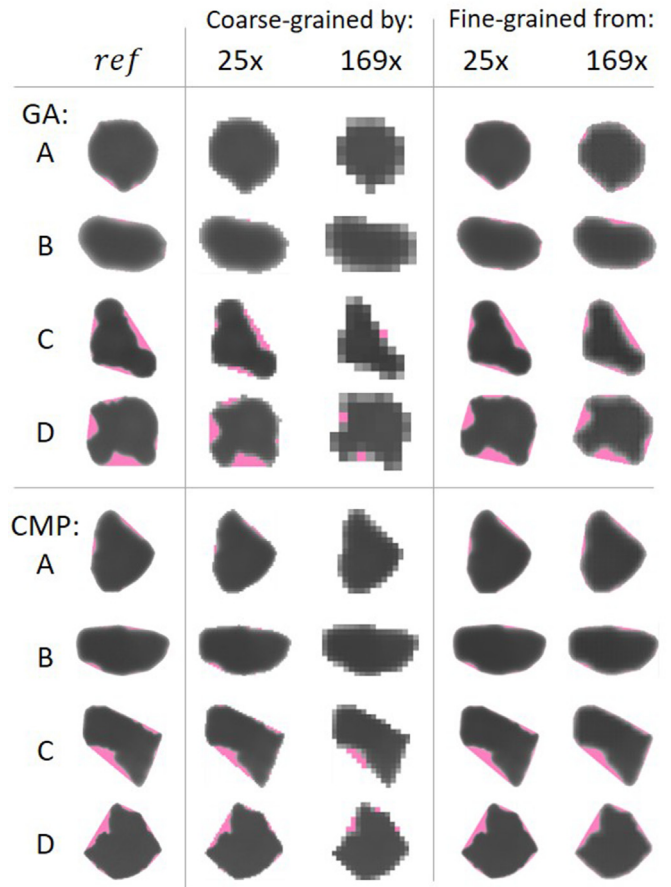


Fig. 8. Examples of coarse graining and machine-learning reconstruction (fine-graining) of thresholded images: particles A–D for each sample are represented on shape maps in Fig. 6.

Table 3

Summary of coarse- and fine-graining shape effects for selected (ref A–D, Fig. 6(a)) gas-atomized (GA) particles.

GA	A			B			C			D		
	EFF	AR _{box}	ϵ_{tra}	EFF	AR _{box}	ϵ_{tra}	EFF	AR _{box}	ϵ_{tra}	EFF	AR _{box}	ϵ_{tra}
ref	0.95	0.91	1.7%	0.96	0.59	1.2%	0.77	0.61	14.5%	0.72	0.89	15.9%
Coarse graining by:												
25x	0.94	0.99	0.0%	0.95	0.60	0.3%	0.76	0.62	13.4%	0.75	0.92	14.5%
64x	0.90	0.97	1.4%	0.98	0.61	0.0%	0.82	0.58	7.8%	0.80	0.86	10.9%
169x	0.97	0.85	0.0%	0.97	0.64	0.0%	0.76	0.60	3.1%	0.75	0.89	5.4%
441x	1.10	0.85	0.0%	1.01	0.57	0.0%	1.00	0.63	0.0%	0.89	0.73	0.0%
Fine graining from:												
25x	0.92	0.90	3.0%	0.93	0.58	3.6%	0.74	0.62	16.2%	0.69	0.90	18.4%
64x	0.90	0.88	4.4%	0.95	0.58	3.3%	0.75	0.61	15.1%	0.70	0.88	18.9%
169x	0.92	0.86	3.7%	0.95	0.59	4.8%	0.77	0.62	14.0%	0.72	0.89	17.9%
441x	0.89	1.0	1.7%	0.97	0.57	2.7%	0.81	0.62	11.2%	0.83	0.90	10.1%

EFF = elliptical form factor; AR = aspect ratio; ϵ_{tra} = [open] intraparticle porosity.

CMP sample; these examples were chosen according to modes of the shape distribution described in Table 2.

4.4.1. Pixel-scale resolution of individual particles

Individual reference particles were selected for each sample, covering the shape distribution map (particles A–D in Fig. 6). In Fig. 8, thresholded grayscale images are shown for each reference (A–D) along with the additional convex hull area in pink. Examples of coarse graining by area (25x, 169x) illustrate the effect of pixel-scale resolution on the convex hull. In reference cases having only small amounts of concavity (i.e. A, B; having high EFF on the map), the convex hull area was eliminated by coarse graining. In cases having more concavity (i.e., C, D; low EFF), convex hull persisted but was eventually eliminated by extreme coarse-graining.

In an effort to improve precision of shape descriptors, a fine-graining method was developed using ML; details are provided in Appendix B. Selected fine-graining results are shown in Fig. 8, essentially reconstructing the reference from coarsened states. The effects of coarse graining and numerical reconstruction by fine graining on shape descriptors are summarized in Tables 3 and 4.

Table 4

Summary of coarse- and fine-graining shape effects for selected (ref A–D, Fig. 6(b)) cold mechanical processed (CMP) particles.

CMP	A			B			C			D		
	EFF	AR _{box}	ϵ_{tra}	EFF	AR _{box}	ϵ_{tra}	EFF	AR _{box}	ϵ_{tra}	EFF	AR _{box}	ϵ_{tra}
ref	0.88	0.77	3.4%	0.93	0.55	2.2%	0.77	0.61	13.2%	0.77	0.96	11.0%
Coarse graining by:												
25x	0.87	0.77	2.0%	0.91	0.58	2.0%	0.74	0.62	11.5%	0.76	0.97	9.9%
64x	0.86	0.75	0.0%	0.89	0.59	1.2%	0.76	0.63	11.1%	0.79	1.00	9.6%
169x	0.84	0.83	0.0%	0.94	0.56	0.0%	0.83	0.62	5.7%	0.81	0.99	5.6%
441x	1.01	0.75	0.0%	0.98	0.55	0.0%	0.73	0.67	9.7%	0.87	0.99	2.5%
Fine graining from:												
25x	0.85	0.76	4.7%	0.90	0.55	3.8%	0.74	0.61	14.4%	0.74	0.94	12.2%
64x	0.86	0.73	3.6%	0.92	0.55	3.5%	0.75	0.61	14.3%	0.76	0.93	11.6%
169x	0.87	0.77	5.2%	0.94	0.55	3.6%	0.77	0.60	13.2%	0.80	0.92	10.6%
441x	0.90	0.88	2.8%	0.95	0.55	2.1%	0.78	0.62	14.4%	0.82	0.91	8.4%

EFF = elliptical form factor; AR = aspect ratio; ϵ_{tra} = [open] intraparticle porosity.

4.4.2. Ensemble effects

Ensemble results for selected shape factors are shown as contour plots, Figs. 9–11. The reference data set had ~7600 particles; the coarse-grained set had ~40,000, combining both GA and CMP samples. The reference line at 1.0 on the ordinate indicates consistency with the raw data; deviation from the 1.0 reference shows the effect of reduced pixel-scale resolution on shape analysis. Coarse-grained data are shown as contour maps, where the color hue corresponds to data density.

Note the vertical dashed line at 5000 (5k) particles indicates the ISO guidance for robust perimeter-based shape measures. Below this, shape analyses inherit uncertainties related to perimeter smoothing and particle orientation. Under-estimation of the perimeter results in over-estimation of form factors; in some cases, illogical form factors (i.e., >1) may result.

Fig. 9 confirms uncertainty related to perimeter smoothing. With NI-Vision, uncertainty is reasonably balanced as low as about 300 pixels; at a lower resolution, a significant skew toward underestimated perimeters (i.e., over-estimated form factors) is observed. Pixel-scale uncertainty also affected aspect ratios (Fig. 10). While the bounding-box ratio was reasonably balanced (Fig. 10(b)), the ISO-defined aspect ratio showed a significant skew

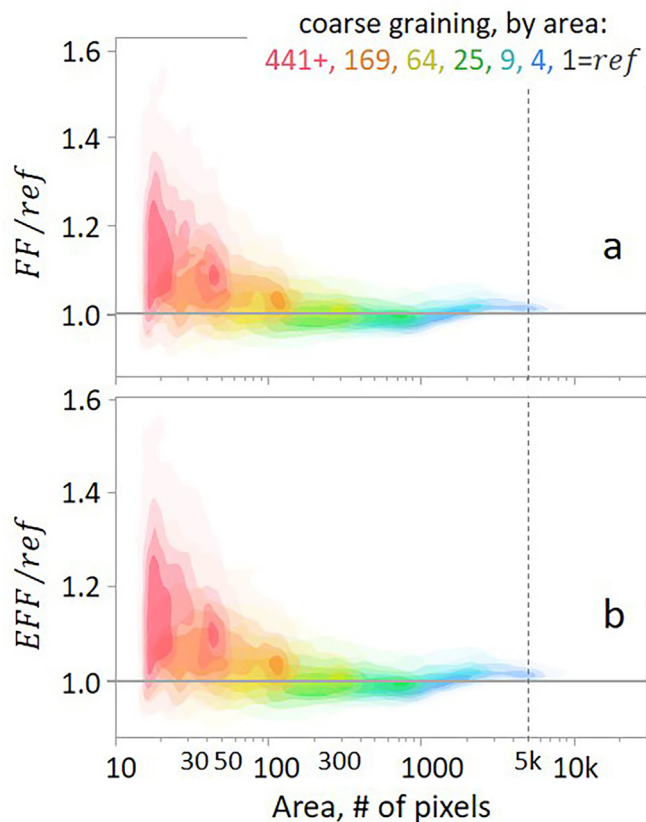


Fig. 9. Coarse-graining analysis of form factors relative to the reference: (a) ISO FF; (b) elliptical FF. ISO = International Standards Organization

with even small amounts of coarse graining. This result suggests a systematic trend toward higher relative maximum Feret lengths with coarser pixilation.

The effect of pixilation on intra-particle porosity derived from Solidity is more profound (Fig. 11). The results were bimodal, showing the porosity estimate of many particles dropping to zero with increasing pixilation, i.e., loss of concavity with pixilation. This effect is most severe with particles having only small amounts of concavity in the reference condition. Concavity was more persistent in reference particles that have more significant reference porosity.

Considering total pore volume, the results in Table 5 represent the summed-up ϵ_{tra} pore volume over the volume-weighted size distributions of each sample. These results show bulk intra-particle porosity derived from concavity having a gradual reduction in the estimated bulk porosity with coarse graining. It means that the bimodal appearance of Fig. 11, while interesting from the perspective of concavity associated with a distribution of individual particles, may be less important to the estimation of cumulative bulk porosity.

An ensemble summary of pixilation uncertainty was evaluated using the standard deviation of each shape factor as a function of the degree of coarse graining in Fig. 12. The relative standard deviation (RSD) was calculated by normalizing the volume-weighted

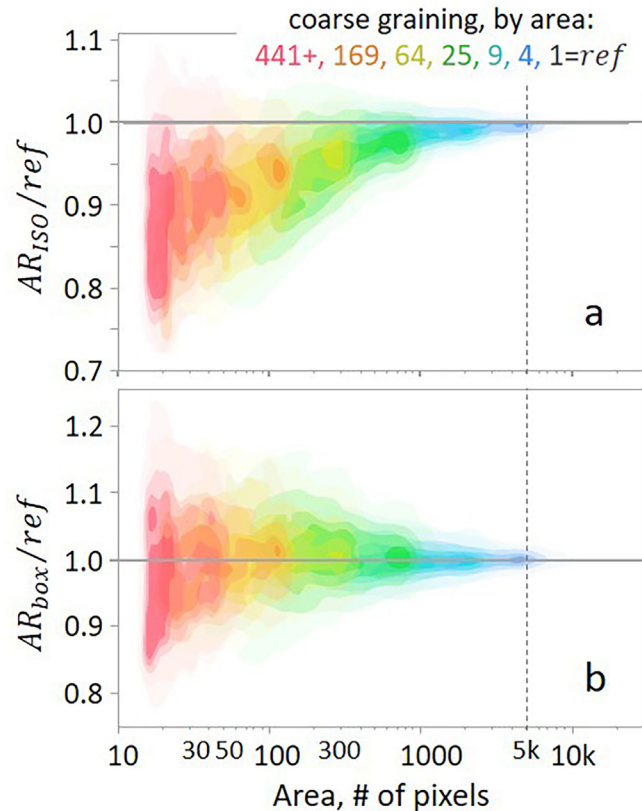


Fig. 10. Coarse-graining analysis of aspect ratios relative to the reference: (a) ISO definition; (b) bounding box ratio. ISO = International Standards Organization

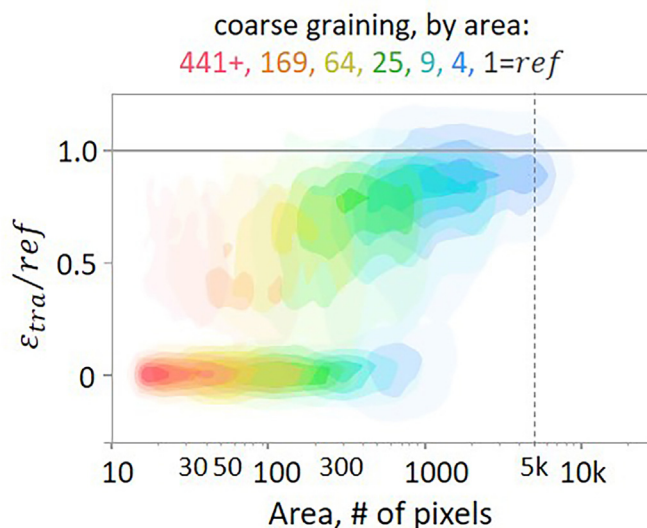


Fig. 11. Coarse-graining analysis of intra-particle porosity relative to reference data.

Table 5
Bulk intraparticle density as a function of coarse graining.

Coarse grain	Bulk ϵ_{tra}	
	GA	CMP
Ref	8.58%	7.26%
4	7.89%	6.72%
9	7.29%	6.26%
25	6.49%	5.67%
64	5.44%	4.81%
169	4.07%	3.63%
441	3.29%	2.40%

CMP = cold mechanical processed; GA = gas atomized.

...

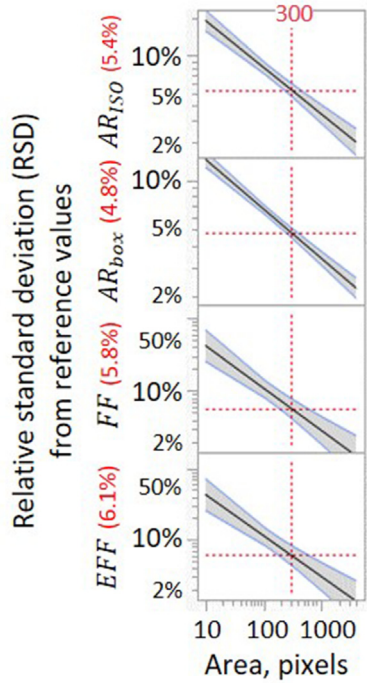


Fig. 12. Shape factor uncertainty shown as relative standard deviation (RSD) from shape factor reference values as a function of pixilation.

standard deviation to the reference. A power law trend is generally followed in Fig. 12, showing RSD uncertainty in the range of about 5%–6% at 300 pixels/particle. Note, the confidence limits are tightest for the bounding-box aspectRatio, AR_{box} , and are marginally looser for the form factors. On the one hand, this is consistent with the ISO guidance regarding uncertainty of perimeter measures; on the other, it suggests opportunities for improved perimeter-measurement algorithms. Results suggest that ML fine-graining can recover porosity and convexity from low-resolution data and enable more consistent perimeter and shape factor calculations.

5. Conclusion

Shape descriptor uncertainty depends on pixilation. For shape distribution statistics, resolution as low as about 300 pixels/particle can provide reasonable accuracy, within a relative standard

deviation of about 5%. The primary limitation is robust calculation of particle perimeters; at low pixel resolution, perimeter calculations are both skewed and variable, resulting in the possibility of illogical form factor values, i.e., FF or $EFF > 1.0$. Applying fine graining via ML can address this problem, maintaining logical form factors and enabling statistically robust shape mapping across broader size ranges.

Shape mapping using aspect ratios and elliptical form factors is consistent with PCA of AM powder datasets, i.e., the elliptical form factor is orthogonal to the aspect ratio. Mapping particles on an AR versus EFF plane decouples perimeter-related irregularities such as bumpiness or angularity from elongation. Superposing particle images on the map is a useful way to visualize differences between samples, for example, the effects of their manufacturing process.

Intra-particle porosity estimates, computed by the way of convex hull, are severely impacted with limited pixel counts. Hence, correlation with solidity under-represents intra-particle porosity at coarse pixel scales. While much of the concavity detail lost in coarse particle images can be recovered through image fine graining, there is a possibility to over-correct compared to reference training data. This begs the question about the need for even higher-resolution reference data in the context of correlating imaging descriptors with porosity. Selective implementation of ML-based image enhancement is a potential way forward toward consistency of shape analysis over broader ranges of particle size.

Declaration of competing interest

The authors declare that they have no known competing financial interests or personal relationships that could have appeared to influence the work reported in this paper.

Acknowledgement

This work was done as independent research – no grant or primary funding was involved.

Appendix A. Derivation of elliptical form factor

The elliptical form factor is analogous to the ISO-defined form factor (ISO, 2008) with the difference being that it compares the measured perimeter to an area-equivalent ellipse instead of a circle. The standard definition of the form factor is $FF = 4\pi A/P^2$, where A is the area, and P is the perimeter as measured using the Cauchy–Crofton method or equivalent. The elliptical form factor uses an approximation for the elliptical perimeter, Eq. (A1) (Vilhelm, 1969), where a and b are the [orthogonal] semi-axes of

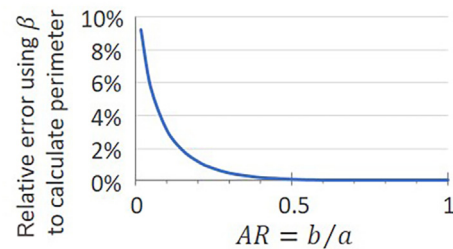


Fig. A1. Relative error of perimeter calculation used in the definition of EFF .

the ellipse. This simple approximation is useful for particles that are not severely elongated, i.e., $AR_{box} > 0.1$ (Fig. A1).

$$P_{ellipse} \approx \pi \left[1.5(a+b) - \sqrt{ab} \right] \quad (A1)$$

The calculation of the area-equivalent elliptical perimeter can be rewritten in terms of the area and aspect ratio, $AR = b/a$, as follows:

$$AR = \frac{b}{a} = \frac{A}{\pi a} \quad (A2)$$

$$a = \sqrt{\frac{A}{\pi \cdot AR}} \quad (A3)$$

$$b = a \cdot AR \quad (A4)$$

$$P_{ellipse} \approx \pi \left[1.5 \left(\sqrt{\frac{A}{\pi \cdot AR}} \cdot (1 + AR) \right) - \sqrt{\frac{A}{\pi}} \right] = \sqrt{\pi A} \left[\frac{1.5(1 + AR)}{\sqrt{AR}} - 1 \right] \quad (A5)$$

Letting $\beta = \left[\frac{1.5(1 + AR)}{\sqrt{AR}} - 1 \right]^2$, the elliptical form factor is defined as,

$$EFF = \beta \pi A / P^2 \quad (A6)$$

Comparing the perimeter approximation, $P_{ellipse} \approx \sqrt{\beta \pi A}$, to the true perimeter (Figure A1), the relative error is negligible for values of $AR > 0.5$, and less than 4% for $AR > 0.1$, which is within the practical domain for many applications of particle shape characterization.

Appendix B. Machine learning for particle image fine-graining

Limited pixel count has been shown to diminish the accuracy of computed shape factors critical to additive manufacturing powders, such as EFF and solidity. Regression techniques can be used to perform a baseline correction to these shape factors as a function of the number of pixels in the image. For a population of particles, this corrects the center of the distribution for a shape factor but still maintains an artificially high amount of variability. To combat the root cause of this issue, ML methods can be used to “fine grain,” or increase the pixel count of the images by inferring from the surrounding pixels a gradient of threshold values across each of the pixels of the original image (Cao, Yao, & Liang, 2020; Wang, Wang, Wang, Li, & Lu, 2020; Xu, 2014). This allows each pixel to be magnified, in this case, by a factor of 100×. A general schematic of neural network architecture is shown in Figure B1.

As illustrated in Figure B2, a 3×3 convolutional window is iterated pixel by pixel across the coarse particle image. The gradient of threshold values for the center pixel is predicted by the algorithm. High-resolution training images obtained from the In-Flow were coarse grained to produce the training and test datasets. The performance of the neural network is shown in Figure B3 as predicted vs the actual grayscale value for each of the magnified center pixel values.

In this study, 10,000 particle images were used in the model training set, and 2500 images were used in the validation set. The characteristics of the particle size and shape distribution are critical in determining the procedures for training a deconvolutional model. When creating training data for the ML model, it is important to utilize high-resolution images that reflect the distribution in particle size, perimeter irregularity (EFF), and elongation (AR) of the particles. High-resolution images can have been quantified as over 5000 pixels per particle, meaning that there is negligible difference

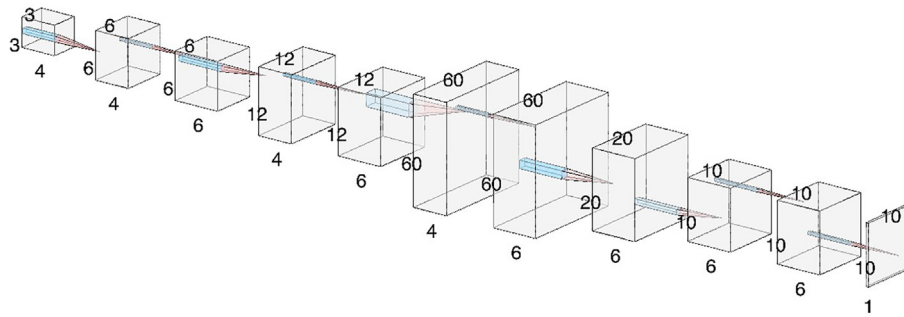


Fig. B1. Neural network architecture, composed of deconvolutional and convolutional layers.

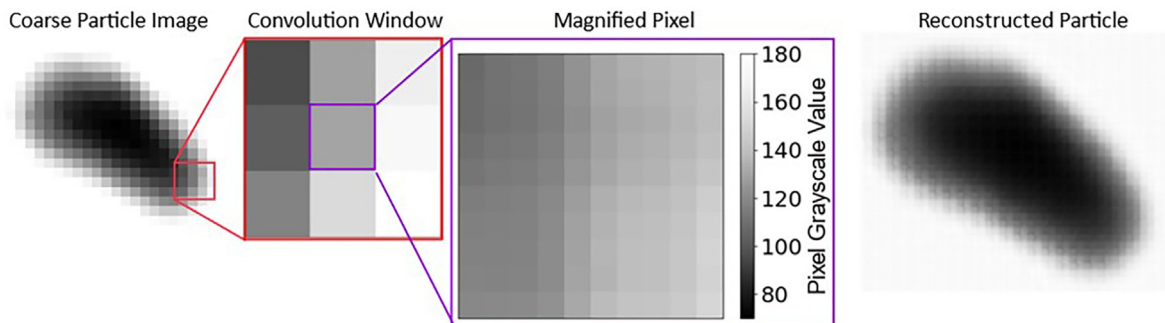


Fig. B2. Convolutional window is input to the neural network, yielding a gradient of threshold values across the center pixel.

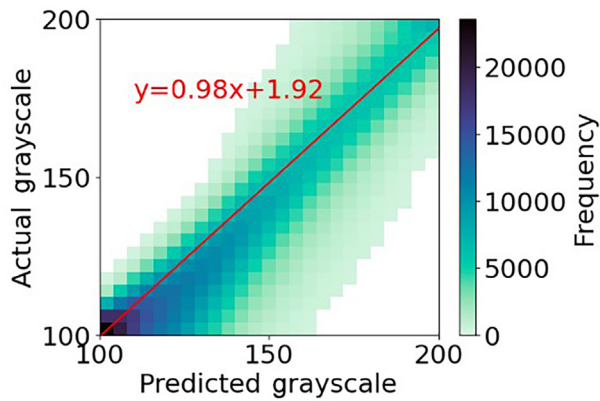


Fig. B3. Parity plot of predicted vs actual pixel gray scale.

in computed size and shape factors, regardless of orientation (ISO, 2008). This ensures that the resulting ML model will be able to predict significant differences in the shapes across the breadth of the size distribution.

In principle, ML fine graining can be applied to any particle type and imaging system, with the recommendation of training the fine-graining model for each type of particle investigated. Particles manufactured in different ways can have different archetypal features that can be recognized and resolved by ML. A test for similarity between particle types can be in the comparison of orthogonal shape features that describe variation in sample shape, for example, *EFF* and *AR* distributions.

References

- Anderson, I. E., White, E. M., & Dehoff, R. (2018). Feedstock powder processing research needs for additive manufacturing development. *Current Opinion in Solid State & Materials Science*, 22(1), 8–15. <https://doi.org/10.1016/j.cossms.2018.01.002>
- Barnes, J., & Aldridge, C. (2019). *System and method for manufacturing powders from ductile materials*. US Patent No. US20210146442A1.
- Cao, F., Yao, K., & Liang, J. (2020). Deconvolutional neural network for image super-resolution. *Neural Networks*, 132, 394–404. <https://doi.org/10.1016/j.neunet.2020.09.017>
- Daugmaudis, J., Laurynėnas, A., & Ivanauskas, F. (2010). The influence of bounding surface on the precision of the Cauchy–Crofton method. *Lietuvos-Matematikos-Rinkiny*, 51, 250–255. <https://doi.org/10.15388/LMR.2010.46>
- Đuriš, M., Arsenijević, Z., Jaćimovski, D., & Kaluderović Radoičić, T. (2016). Optimal pixel resolution for sand particles size and shape analysis. *Powder Technology*, 302, 177–186. <https://doi.org/10.1016/j.powtec.2016.08.045>
- ISO. (2008). *Representation of results of particle size analysis. Part 6, Descriptive and quantitative representation of particle shape and morphology*. ISO 9276-6:2008. British Standards Institution.
- Kim, Y., Suh, H. S., & Yun, T. S. (2019). Reliability and applicability of the Krumbein–Sloss chart for estimating geomechanical properties in sands. *Engineering Geology*, 248, 117–123. <https://doi.org/10.1016/j.enggeo.2018.11.001>
- Kröner, S., & Doménech Carbó, M. T. (2013). Determination of minimum pixel resolution for shape analysis: Proposal of a new data validation method for computerized images. *Powder Technology*, 245, 297–313. <https://doi.org/10.1016/j.powtec.2013.04.048>
- Krumbein, W. C., & Sloss, L. L. (1951). *Stratigraphy and sedimentation*. San Francisco: Freeman.
- Martin, J., Barnes, J., Rogers, K., Hundley, J., LaPlant, D. L., Ghanbari, S., et al. (2023). Additive manufacturing of a high-performance aluminum alloy from cold mechanically derived non-spherical powder. *Communications Materials*, 4(39), 1–7. <https://doi.org/10.1038/s43246-023-00365-4>
- MATLAB. (2023). Computer vision toolbox. www.mathworks.com/products/computer-vision.html&dummy. (Accessed 23 July 2023).
- MorphoLibJ. (2023). MorphoLibJ. <https://imagej.net/plugins/morpholibj>.
- Mort, P. (2022). Analysis and graphical representation of particle size distributions. *Powder Technology*, 420, 1–11. <https://doi.org/10.1016/j.powtec.2022.118100>
- Muniz-Lerma, J. A., Nommeets-Nomm, A. W., & Brochu, M. (2018). A comprehensive approach to powder feedstock characterization for powder bed fusion additive manufacturing: A case study on AlSi7Mg. *Materials*, 11(12), 1–15. <https://doi.org/10.3390/ma11122386>
- NI-Vision. (2023). Particle measurements - NI, 05_01 www.ni.com/docs/en-US/bundle/ni-vision-concepts-help/page/particle_measurements.html. (Accessed 13 July 2023).
- Pirard, E. (2004). Image measurements. In P. Francus (Ed.), *Image analysis, sediments and paleoenvironments* (pp. 59–86). Springer.
- Pons, M.-N., & Dodds, J. (2015). In S. Tarleton (Ed.), *Progress in filtration and separation, chapter fifteen - particle shape characterization by image analysis*. Academic Press. <https://doi.org/10.1016/B978-0-12-384746-1.00015-X>
- Shaheen, M. Y., Thornton, A. R., Luding, S., & Weinhart, T. (2021). The influence of material and process parameters on powder spreading in additive manufacturing. *Powder Technology*, 383, 564–583. <https://doi.org/10.1016/j.powtec.2021.01.058>
- Slotwinski, J. A., Garboczi, E. J., & Hebenstreit, K. M. (2014). Porosity measurements and analysis for metal additive manufacturing process control. *Journal of Research of the National Institute of Standards and Technology*, 119, 494–528. <https://doi.org/10.6028/jres.119.019>
- Spierings, A. B., Herres, N., & Levy, G. (2011). Influence of the particle size distribution on surface quality and mechanical properties in AM steel parts. *Rapid Prototyping Journal*, 17(3), 195–202. <https://doi.org/10.1108/13552541111124770>
- Vilhelm, V. (1969). Chapter 3, Some Formulae (areas, circumferences, volumes, surfaces, centroids, moments of inertia). In K. Rektorys (Ed.), *Survey of applicable mathematics*. Cambridge: MIT Press.
- Wang, Y., Wang, L., Wang, H., Li, P., & Lu, H. (2020). Blind single image super-resolution with a mixture of deep networks. *Pattern Recognition*, 102, 1–11. <https://doi.org/10.1016/j.patcog.2019.107169>
- Weaver, J. S., Whiting, J., Tondare, V., Beauchamp, C., Peltz, M., Tarr, J., et al. (2021). The effects of particle size distribution on the rheological properties of the powder and the mechanical properties of additively manufactured 17-4 PH stainless steel. *Additive Manufacturing*, 39, 1–18. <https://doi.org/10.1016/j.addma.2021.101851>
- Xu, L. R. (2014). Deep convolutional neural network for image deconvolution. www.lxu.me/projects/dcnv/.
- Zheng, J., & Hryciw, R. D. (2015). Traditional soil particle sphericity, roundness and surface roughness by computational geometry. *Géotechnique*, 65(6), 494–506. <https://doi.org/10.1680/geot.14.P.192>